Polarization transfer to bound protons measured by quasielastic electron scattering on ¹²C

Tilen Brecelj, ^{1,*} Sebouh J. Paul ^{0,2,*,†} Tim Kolar, ¹ Patrick Achenbach, ³ Adi Ashkenazi, ² Ralph Böhm, ³ Erez O. Cohen, ² Michael O. Distler, ³ Anselm Esser, ³ Ronald Gilman, ⁴ Carlotta Giusti, ⁵ David Izraeli, ² Igor Korover, ^{6,2} Jechiel Lichtenstadt, ² Israel Mardor, ^{2,7} Harald Merkel, ³ Miha Mihovilovič, ^{8,1,3} Ulrich Müller, ³ Mor Olivenboim, ² Eli Piasetzky, ² Guy Ron, ⁹ Björn S. Schlimme, ³ Matthias Schoth, ³ Florian Schulz, ³ Concettina Sfienti, ³ Simon Širca, ^{8,1} Samo Štajner, ¹ Steffen Strauch, ¹⁰ Michaela Thiel, ³ Adrian Weber, ³ and Israel Yaron²

(A1 Collaboration)

¹ Jožef Stefan Institute, 1000 Ljubljana, Slovenia ² School of Physics and Astronomy, Tel Aviv University, Tel Aviv 69978, Israel

³Institut für Kernphysik, Johannes Gutenberg-Universität, 55099 Mainz, Germany ⁴Rutgers, The State University of New Jersey, Piscataway, New Jersey 08855, USA

*Dipartimento di Fisica, Università degli Studi di Pavia and INFN, Sezione di Pavia, Nel Bassi 6, I-27100 Pavia, Italy

⁶Department of Physics, NRCN, P.O. Box 9001, Beer-Sheva 84190, Israel

⁷Soreg NRC, Yavne 81800, Israel

Faculty of Mathematics and Physics, University of Ljubljana, 1000 Ljubljana, Slovenia
 Racah Institute of Physics, Hebrew University of Jerusalem, Jerusalem 91904, Israel
 University of South Carolina, Columbia, South Carolina 29208, USA



(Received 1 March 2020; accepted 1 May 2020; published 17 June 2020)

We report the measurements of the transverse (P'_x) and longitudinal (P'_z) components of the polarization transfer to a bound proton in carbon via the quasifree $^{12}C(\vec{e},e'\vec{p})$ reaction, over a wide range of missing momenta. We determine these polarization transfers separately for protons knocked out from the s and p shells. The electron-beam polarization was measured to determine the individual components with systematic uncertainties which allow a detailed comparison with theoretical calculations.

DOI: 10.1103/PhysRevC.101.064615

I. INTRODUCTION

Polarization transfer from a polarized electron to a proton in elastic scattering has become a recognized method to measure the proton's elastic electromagnetic form factors, G_E and G_M [1–9]. Assuming the one-photon exchange approximation, the ratio of the transverse (P_x') to longitudinal (P_z') polarization-transfer components is proportional to the ratio of these form factors, G_E/G_M [10]. This provides a direct measurement of the form factor (FF) ratio, even under conditions where one of the FFs is much larger than the other, and eliminates many systematic uncertainties [11].

Measuring the ratio of the components of the polarization transfer to a *bound* proton in *quasifree* kinematics on nuclei, which is sensitive to the electromagnetic FF ratio, has been suggested as a method to study differences between free and bound protons [4,5]. As such it can be used as a tool to identify medium modifications in the bound proton's internal structure, reflected in the FFs and thereby in the polarization transfer. Deviations between measured polarization ratios in quasifree $A(\vec{e}, e'\vec{p})$ and elastic $\vec{e}p$ scattering can be interpreted only by comparing the measurements with realistic calculations of nuclear effects such as final-state interactions (FSI).

Polarization-transfer experiments have been carried out on 2 H and 12 C target nuclei at the Mainz Microtron (MAMI) [12–15], as well as on 2 H, 4 He, and 16 O at Jefferson Lab (JLab) [16–18], in search of medium modification in the proton internal structure. These experiments were performed to study deeply bound nucleons, characterized by high missing momentum which is equivalent (neglecting FSI) to protons with high initial momentum. It was shown for the 2 H measurements that the deviations in P_x'/P_z' from that of elastic $\vec{e}p$ scattering can be explained by nuclear effects without the necessity of introducing modified FFs [12–14]. Furthermore, when comparing the quasielastic polarization transfer to that of elastic $\vec{e}p$ scattering, the double ratio $(P_x'/P_z')^A/(P_x'/P_z')^{^1}$ H exhibits a very similar behavior for 2 H [12,14,17], 4 He [18], and 12 C [15], suggesting a universality.

While the ratio of the components is better determined experimentally than the individual components (smaller systematic uncertainties), it is insensitive to possible common effects to P'_x and P'_z which cancel in the ratio. To test calculations in better detail, and further corroborate their reliability, measurements of individual components of the polarization transfer are required.

The polarization-transfer components have previously been measured for ²H at MAMI [13,14,19], as well as ⁴He at JLab [18]. For ²H, statistically significant but relatively small deviations were observed between the measured components and the predicted values, but not in their ratio [13,14].

^{*}These authors contributed equally to this work.

[†]Corresponding author: paulsebouh@mail.tau.ac.il

The ¹²C nucleus is a particularly appealing target for such studies as one can selectively probe protons from specific nuclear shells, *s* and *p*. The average local densities in these shells differ by about a factor of 2, which was predicted to impact the polarization transfer to *s*- and *p*-shell protons differently [20]. If modifications to the bound-proton structure by the nuclear medium exist, and are reflected in the proton FFs, then they may depend either on the off-shellness of the bound proton (virtuality), or on the local nuclear density, or both. Therefore, it is important to measure the components of the polarization transfer in both shells over a large missingmomentum range and to have reliable calculations for them in order to identify modifications which can be related to the FFs.

In this work, we present measurements of the $^{12}\mathrm{C}(\vec{e},e'\vec{p})$ reaction at MAMI over a wide range of missing momentum of the struck proton. The beam-polarization determination had a sufficient accuracy for extracting the individual polarization-transfer components P'_x and P'_z and for allowing a meaningful comparison with theoretical calculations. The results of the measured ratio P'_x/P'_z have been reported in [15]. The new analysis presented here includes improvements in the corrections for the energy loss of the particles when exiting the target, as well as the polarization-extraction procedure.

Section II describes the experimental setup, including the beam line, target, and spectrometers. Details of the measured reaction and its kinematics are given in Sec. III. The data analysis and determination of the polarization components are described in Sec. IV. Finally, in Sec. V, we interpret the data, compare them to a set of calculations, and explore the sensitivity to the proton FFs.

II. EXPERIMENTAL SETUP

The experiment was performed at MAMI using the beam line and spectrometers of the A1 Collaboration [21]. We used a 600 MeV continuous-wave polarized electron beam with a current of about 10 μ A and an \approx 80% polarization. The beam helicity was flipped at a rate of 1 Hz in order to reduce time-dependent systematics in the polarization-transfer measurements.

The beam polarization was measured with a Møller polarimeter [22,23] about twice daily, and verified by a Mott polarimetry measurement [24] taken at the start of the measurement period. These two methods of beam-polarization measurement produced mutually consistent results, as shown in Fig. 1, and each had a systematic uncertainty of 2%.

In between taking the two datasets at different kinematic settings, we refreshed the GaAs crystal in the polarized beam source. This resulted in a drop in the beam polarization from 82.6% to 79.1%. These values reflect the average beampolarization measurements before and after the crystal was refreshed. During the data-taking, the beam polarization remained constant within error.

The target consisted of three carbon (graphite) foils of 0.8 mm thickness each, separated by about 15 mm and tilted at an angle of 40° with respect to the beam. Their transverse dimensions were 4 mm \times 20 mm, as shown in Fig. 2. This design reduced the distance that the protons would travel

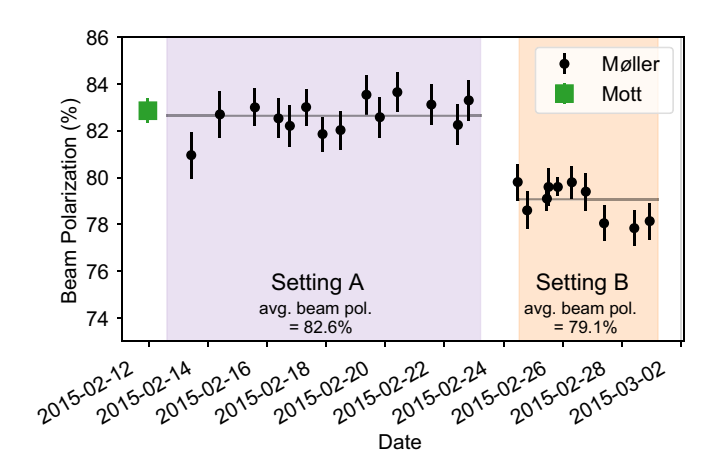


FIG. 1. The measured beam polarizations using the Møller (black circles) and Mott (square, green) polarimeters. The average beam polarizations for each dataset are shown as horizontal lines. The error bars shown are statistical errors, and do not include systematic errors, estimated to be around 2% for both the Møller and Mott polarimeters. The shaded regions represent the data-taking periods for the two kinematic settings of the experiment.

through the target foils, both by using multiple foils (rather than a single thick foil) and by rotating each foil such that the detected protons would exit nearly normal to the foil. This reduced their energy loss in the target. It also improved the resolution for the reaction-vertex determination, consequently reducing the systematic uncertainty in the measured polarization-transfer components at the reaction point.

Two high-resolution, small-solid-angle spectrometers with momentum acceptances of 20–25% were used to detect the scattered electrons in coincidence with the knocked-out protons. Each of these spectrometers consists of a magnet system with a quadrupole-sextupole-dipole-dipole configuration,

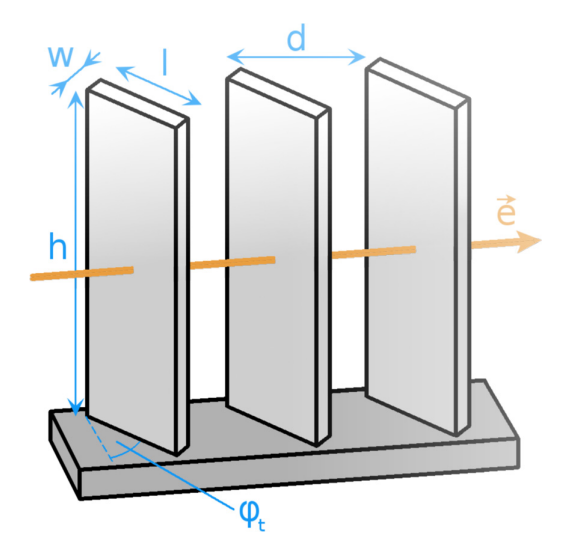


FIG. 2. Schematic view of the carbon target, consisting of three graphite foils. The thick arrow (orange) indicates the direction of the electron beam. The dimensions shown are $h \times l \times w = 20$ mm \times 4 mm \times 0.8 mm, d=15 mm, and $\phi_l=40^\circ$.

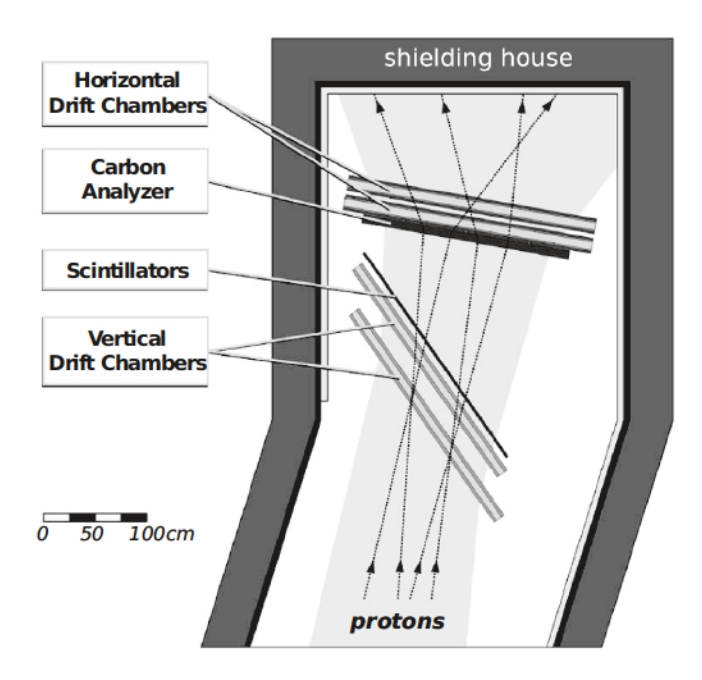


FIG. 3. Side view of the detector system of the proton spectrometer. The standard detector system (VDCs and scintillators) is supplemented by the FPP, which consists of a carbon analyzer and two double planes of HDCs for proton tracking after scattering in the carbon analyzer. Some proton trajectories are indicated within the region of acceptance (shaded area). Adapted from [25].

followed by vertical drift chambers (VDCs) for tracking, and a scintillator system for triggering and the timing coincidence between the two spectrometers. The electron spectrometer also includes a Čerenkov detector for identifying electrons and distinguishing them from background particles such as π^- and cosmic rays.

The proton spectrometer was equipped with a focal-plane-polarimeter (FPP) consisting of a 7 cm thick carbon analyzer [21,25] and horizontal drift chambers (HDCs) to measure the secondary scattering of the proton in the analyzer, as shown in Fig. 3. The spin-dependent scattering of the polarized proton by the carbon analyzer enables the determination of the proton's transverse polarization components at the focal plane [25]. The polarization-transfer components at the *reaction* point were obtained by transforming the measured components using the known spin precession in the magnetic field of the spectrometer.

III. MEASURED REACTION AND KINEMATICS

The kinematics of the measured reaction are shown in Fig. 4. The electron's initial and final momenta are \vec{k} and \vec{k}' respectively, and they define the scattering plane of the reaction. The proton's initial momentum introduces, in addition, the reaction plane defined by the momentum transfer $\vec{q} = \vec{k} - \vec{k}'$ and the exiting proton's momentum \vec{p}' . The angle between the scattering plane and the reaction plane is denoted by ϕ_{pq} .

Following the convention of [16], we express the components of the polarization transfer \vec{P}' in the scattering-plane coordinate system, where \hat{z} is along the direction of the

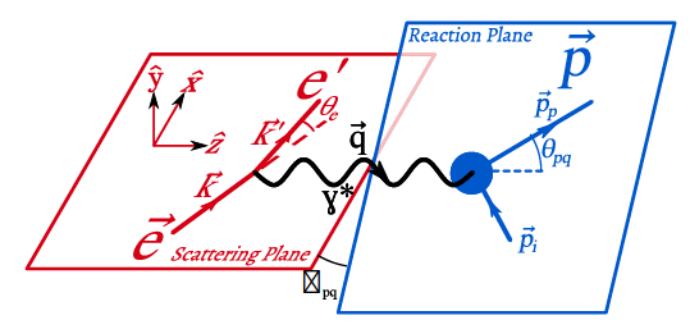


FIG. 4. Kinematics of the measured reaction.

momentum transfer \vec{q} , \hat{y} is along the direction of $\vec{k} \times \vec{k}'$, and $\hat{x} = \hat{y} \times \hat{z}$, forming a right-handed coordinate system.

The missing momentum $\vec{p}_{\text{miss}} = \vec{q} - \vec{p}'$ is the recoil momentum of the residual nucleus. Neglecting FSI, $-\vec{p}_{\text{miss}}$ is equal to the initial momentum of the emitted proton. We conventionally define positive and negative signs for p_{miss} as the sign of $\vec{p}_{\text{miss}} \cdot \vec{q}$.

Our data were taken at two kinematic settings, A and B, covering different ranges in $p_{\rm miss}$ at different invariant four-momentum transfers, $Q^2 = -q^2$. Setting A was centered near $p_{\rm miss} = 0$, at $Q^2 = 0.40~({\rm GeV}/c)^2$. Setting B covered a region of large negative $p_{\rm miss}$, at $Q^2 = 0.18~({\rm GeV}/c)^2$. The details of these kinematic settings are given in Table I.

Following [26], we distinguish between protons knocked out from the s and p shells using cuts on the missing energy, E_{miss} in the reaction, defined as

$$E_{\text{miss}} \equiv \omega - T_p - T_{1}_{B}, \tag{1}$$

where $\omega = k^0 - k'^0$ is the energy transfer, T_p is the measured kinetic energy of the outgoing proton, and $T_{^{11}B}$ is the calculated kinetic energy of the recoiling ^{11}B nucleus. The measured $E_{\rm miss}$ spectrum is shown in Fig. 5. For the s-shell sample we used the cut $30 < E_{\rm miss} < 60$ MeV, while for the p-shell sample we used $15 < E_{\rm miss} < 25$ MeV [15]. Also shown in Fig. 5 are the $p_{\rm miss}$ spectra for the two shells.

When protons are knocked out from the p shell of the carbon nucleus, the A-1 system is left in a discrete state

TABLE I. The kinematic settings in the $^{12}\text{C}(\vec{e}, e'\vec{p})$ experiment. The angles and momenta represent the central values for the two spectrometers: p_p and θ_p (p_e and θ_e) are the knocked out proton (scattered electron) momentum and scattering angles, respectively.

		Kinematic setting		
		A	В	
E_{beam}	(MeV)	600	600	
Q^2	$[(\text{GeV}/c)^2]$	0.40	0.18	
$p_{ m miss}$	(MeV/c)	-130 to 100	-250 to -100	
p_e	(MeV/c)	385	368	
θ_e	(deg)	82.4	52.9	
p_p	(MeV/c)	668	665	
$egin{array}{c} p_p \ heta_p \end{array}$	(deg)	-34.7	-37.8	
No. of events after cuts		1.7×10^6	1.1 ×10 ⁶	

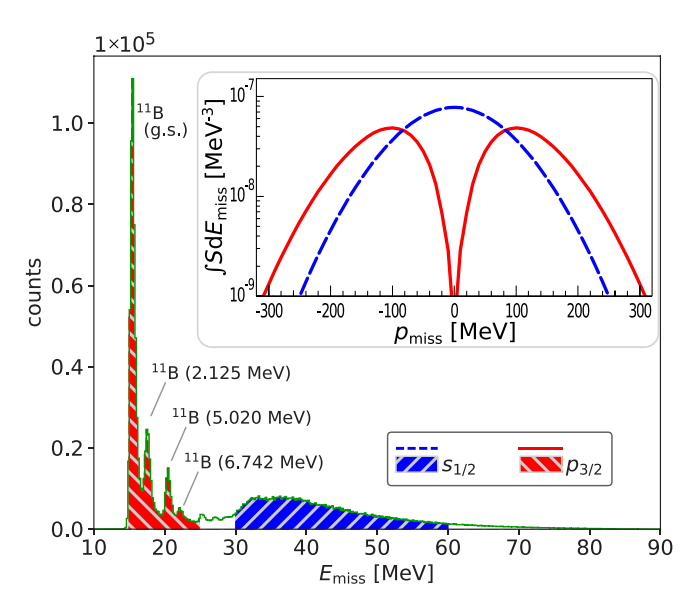


FIG. 5. The measured proton missing-energy spectrum for $^{12}\text{C}(\vec{e},e'\vec{p})$ (data shown are for Setting A). The distinct peaks correspond to removal of $p_{3/2}$ -shell protons in ^{12}C resulting in ^{11}B ground state and excited states as noted. The E_{miss} ranges considered in the analysis for $p_{3/2}$ and $s_{1/2}$ protons are marked in red and blue, respectively. The inset shows the momentum distribution predictions of the independent-particle shell model for $p_{3/2}$ and $s_{1/2}$ protons in ^{12}C , adapted from [26].

(either the ground state or one of the excited states of 11 B). However, knockout from the *s* shell leaves the residual A-1 system unbound, leading to a continuum of residual states. The wave function at p=0 has a minimum for the *p* state and a maximum for the *s* state (see inset of Fig. 5).

An important quantity characterizing the proton prior to its knockout is its "off-shellness." We quantify this using the virtuality, ν , a variable defined as [12]

$$\nu \equiv \left(M_A c - \sqrt{M_{A-1}^2 c^2 + p_{\text{miss}}^2}\right)^2 - p_{\text{miss}}^2 - M_p^2 c^2, \tag{2}$$

where M_A is the mass of the target nucleus, $M_{A-1} \equiv \sqrt{(\omega - E_p + M_A c)^2 - p_{\text{miss}}^2}$ is the mass of the residual nucleus (not necessarily in its ground state) determined event by event, and E_p is the total energy of the outgoing proton. We note that the virtuality depends not only on p_{miss} but also on M_{A-1} . The minimum value of |v| (for a given target nucleus) is

$$|\nu|_{\min} = (M_p^2 - (M_A - M_{A-1}^{g.s.})^2)c^2,$$
 (3)

where $M_{A-1}^{\rm g.s.}$ is the ground-state mass of the the residual nucleus (in this case, ¹¹B). For the ¹²C(\vec{e} , $e'\vec{p}$) ¹¹B reaction, $|\nu|_{\rm min}=0.0297~({\rm GeV}/c)^2$. Protons knocked out from the s shell are generally further off shell than those in the p shell (even in events at the same $p_{\rm miss}$, due to their larger $E_{\rm miss}$).

IV. DATA ANALYSIS

A. Event reconstruction and selection

For the event reconstruction, we used the COLA++ reconstruction framework [27], developed by the A1 Collaboration.

The reconstructed angles and positions of the tracks at the VDC plane are used in a fit to find the initial momentum, angle, and vertex position of each particle. A multivariate polynomial fit is then used to reconstruct the proton's spin-transfer matrix (STM) for each event.

Software cuts were then applied to the data. We require the time coincidence between the scintillators of the two spectrometers to be within a ± 5 ns window, and that the signal in the Čerenkov detector be above the electron-detection threshold. We include tracking cuts which ensure good tracking in the spectrometers and require that both the electron and the proton originate from the carbon target. Further tracking cuts require the proton's trajectory to be within the part of the spectrometer where the precession of the proton's spin is well known.

In the FPP, we removed events with (spin-independent) Coulomb scattering in the carbon analyzer by selecting only events where the proton scattered by more than 8°. We also required the fitted position of the scattering point in the FPP (determined by the HDC and the extrapolated trajectory from the VDC) to be consistent with the actual position of the analyzer.

B. Polarization fitting

There are two types of polarization observables that can be obtained in this experimental setup: the induced polarization \vec{P} (which is the proton polarization for an unpolarized electron beam) and the polarization transfer \vec{P}' (which determines the beam polarization-dependent part of the proton polarization). The total outgoing proton polarization is related to these observables via

$$\vec{P}_{n,\text{tot}} = \vec{P} + hP_e\vec{P}',\tag{4}$$

where h and P_e are the helicity and polarization of the electron beam

We perform a fit to obtain \vec{P} and \vec{P}' by maximizing the log-likelihood

$$\ln \mathcal{L} = \sum_{k} \ln(1 + \vec{P}_{p,\text{tot}} \cdot \vec{\lambda}_k), \tag{5}$$

where the $\vec{\lambda}_k$ for each event are given by

$$\vec{\lambda}_k = a\mathbf{S}^{-1} \begin{pmatrix} -\sin\phi_{\text{FPP}} \\ \cos\phi_{\text{FPP}} \\ 0 \end{pmatrix}, \tag{6}$$

and ϕ_{FPP} is the measured azimuthal scattering angle in the FPP. S is the calculated spin-transfer matrix for the event and a is the analyzing power of the event (as determined in [28,29]).

Three of these components $(P_x, P_y', \text{ and } P_z)$ are expected to be very small for individual events and antisymmetric in their dependence on ϕ_{pq} [30]. Hence, they would average to zero when considering event samples that have symmetric distributions in ϕ_{pq} , as is nearly the case in our dataset. Therefore, in order to improve the stability of our fit, we fix

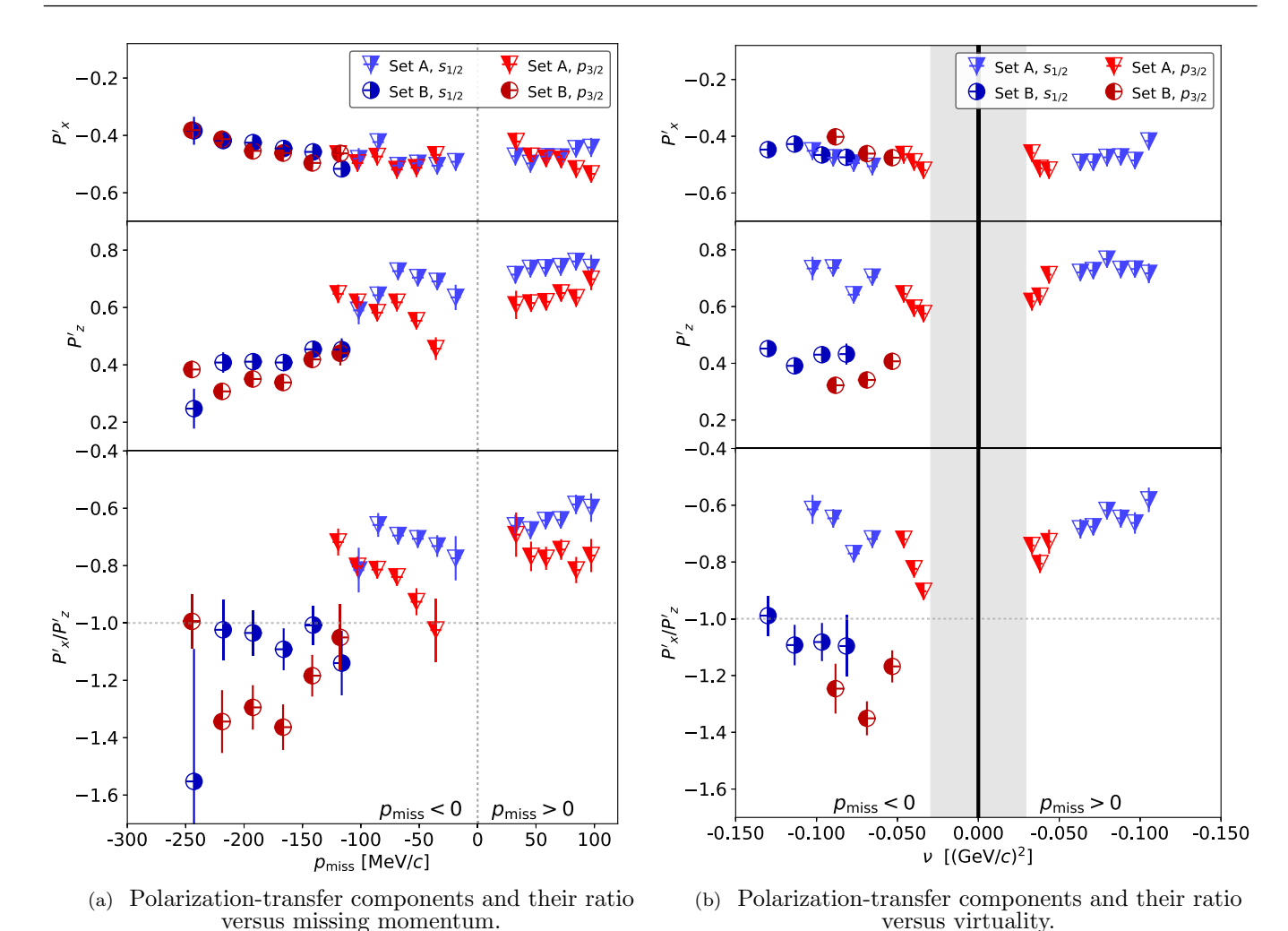


FIG. 6. The measured polarization-transfer components, P_x' (top), P_z' (middle), and their ratio, P_x'/P_z' (bottom). These are plotted versus the missing momentum (a) and virtuality (b). In the virtuality plot (b), the data with positive (negative) p_{miss} are shown separately. The grey band shows the kinematically forbidden region at |v| < 0.0297 (GeV/c)² [see Eq. (3)]. The uncertainties shown are statistical only. Systematic errors are discussed in Sec. IV C. Triangles (circles) refer to kinematic Setting A (B). Symbols that are open on the left (right) side refer to s-shell (p-shell) removals, and are colored blue (red). The legend is common to all panels in the figure.

these parameters to zero, leaving us with

$$\vec{P}_{p,\text{tot}} = \begin{pmatrix} h P_e P_x' \\ P_y \\ h P_e P_z' \end{pmatrix}. \tag{7}$$

We partitioned both the s- and p-shell knockout data into bins by $p_{\rm miss}$, and performed the above procedure on each bin separately, the results of which are shown in Fig. 6(a). Likewise, we binned the data by the virtuality, and show the results in Fig. 6(b). We present the results binned by both variables to show how the polarization may vary with the protons' motion ($p_{\rm miss}$ bins) and also their off-shellness (virtuality bins). This avoids conflating effects related to one variable with those related to the other, as the two are correlated.

C. Systematic uncertainties in the measurements

The systematic errors in these measurements are due to a few sources, which are presented in Table II. The largest con-

TABLE II. Systematic uncertainties of P'_x , P'_z and P'_x/P'_z . All values are in percent. See text for details.

	dP_x'/P_x'	dP_z'/P_z'	$\frac{d[P_x'/P_z']}{P_x'/P_z'}$
Beam polarization	2.0	2.0	0.0
Analyzing power	1.0	1.0	0.0
Beam energy	0.2	0.6	0.8
Central kinematics	0.6	0.8	0.9
Alignment	< 0.1	0.1	0.1
Software cuts	1.7	2.1	1.9
Precession (STM fit)	0.3	0.3	0.3
Precession (trajectory)	0.2	0.3	< 0.1
Total	2.9	3.3	2.3

¹We have also performed the fit with all six parameters included, and have found that this does not strongly affect the outcome of the fit except in bins with poor statistics.

tribution to the uncertainty in the polarization components P'_x and P'_z is due to the beam polarization, which was determined with an estimated uncertainty of 2%. These components are also sensitive to the analyzing power of the carbon secondary scatterer, which in this kinematic region is known to about 1% [25,28,29]. However, the ratio P'_x/P'_z is independent of both the beam polarization and the analyzing power.

The uncertainties in the beam energy and the central kinematics of the spectrometers in each dataset affect the basis vectors that define the scattering-plane coordinate system, as well as which bin an event goes into. The alignment between the HDC coordinate system and the tracks extrapolated from the VDC to the HDC plane also affected the polarization measurement, since these measurements depend on the distribution of the angles of the secondary scattering.

These three sources of uncertainty (beam energy, central kinematics, and detector alignment) were determined in the following manner. We modified each of the variables, one by one, by their uncertainty values, and repeated the analysis, and then determined how much this affected the extracted polarizations. The errors from each source were then added in quadrature.

The systematics due to software cuts were studied by reanalyzing the data with each cut slightly tighter than the actual value that is used in the final analysis and taking the average of the effects of the modified cut over all of the bins. The values in the row labeled "software cuts" in Table II are the quadratic sums of the effects from each of the different cuts

The uncertainty in the spin-precession evaluation was estimated by comparing the STM calculated internally by the COLA++ software in the event reconstruction (which uses a polynomial fit) and a more precise (but much slower) calculation using the QSPIN program [25]. The fit was able to reproduce the spin precession with an uncertainty of 0.3% [25].

Furthermore, the finite resolution of the proton's trajectory parameters, especially the vertex position, adds additional systematic uncertainty to the precession. To begin determining this part of the systematic uncertainty, we used QSPIN to calculate the spin-transfer matrix, \mathbf{S}_{ref} , for a reference trajectory. We then produced 100 other trajectories with normally distributed variations in each parameter, where the standard deviation of each parameter equals the resolution of that parameter, to produce precession matrices \mathbf{S}_i . The resulting uncertainty on the measured polarization due to the trajectory is then

$$\delta \vec{P} = (\mathbf{I}_3 - \operatorname{avg}_i[\mathbf{S}_i]\mathbf{S}_{ref}^{-1})\vec{P}, \tag{8}$$

where I_3 is the 3×3 identity matrix and $avg_i[S_i]$ represents the average of the matrices S_i . The average is performed because the measured polarization is calculated using an ensemble of trajectories, rather than a single trajectory.

The total estimated systematic uncertainties are calculated by adding the effects of each of the individual sources in quadrature. The systematic uncertainties for the individual transfer components P'_x and P'_z are $\approx 3\%$ and the uncertainty for their ratio is $\approx 2\%$. These are consistent with estimates of the systematic uncertainties from previous polarization-

transfer measurements on the deuteron using the same experimental setup and comparable kinematic settings [12–15].

V. INTERPRETATION OF RESULTS

A. General observations

As shown in Fig. 6, the P_x' components are less sensitive to the different kinematic variables, p_{miss} and ν , than P_z' . We find that P_x' is nearly identical for s and p shells at the same p_{miss} . The P_z' component for p-shell knockout dips down at small negative p_{miss} , while this does not seem to be the case in s-shell knockout.

We observe that where the two kinematic settings overlap in virtuality there is no regularity in P'_z , and that P'_z is much larger at Setting A than at Setting B.

In order to further interpret our polarization-transfer data, we compare them to dedicated calculations of $^{12}\text{C}(\vec{e}, e'\vec{p})$ described in Sec. VB below.

B. Calculations of the polarization transfer for ¹²C

We compared the measured polarization transfer to relativistic distorted-wave impulse approximation (RDWIA) calculations [31], where the FSI between the outgoing nucleon and the residual nucleus are described by a phenomenological relativistic optical potential.

In the calculations, the so-called democratic optical potential [32] has been used, which has been obtained using a global fit to over 200 datasets using elastic proton-nucleus scattering over a broad range of nuclei from helium to lead. The differences in the calculated polarization transfer due to the choice of the optical potential were estimated at about 2–4%. The evaluation was done by comparing the results obtained with the democratic and the energy-dependent and atomic-number-independent (EDAI) relativistic optical potential [33], which is a single-nucleus parametrization, constructed to reproduce elastic proton-scattering data just on ¹²C.

The relativistic bound-state wave functions used in the calculations have been obtained by solving the relativistic Hartree-Bogoliubov Equations using the program ADFX [34]. The model is applied in the mean-field approximation to the description of ground-state properties of spherical nuclei, using a Lagrangian containing the σ , ω , and ρ mesons and the photon field [35–38]. Moreover, finite-range interactions are included to describe pairing correlations and the coupling to particle continuum states. The Lagrangian parameters are usually obtained by a fitting procedure to some bulk properties of a set of nuclei. The wave functions used in our calculations were obtained with the NL-SH parametrization [39]. The results of the calculations using different parametrizations differ by about 0.5–0.8%.

The Coulomb distortion of the electron wave functions is considered using the effective-momentum approximation. Our calculation uses the parametrization of the free-proton FFs from [40], which are known to within 0.5% in the kinematic region of our experiment.

In coplanar kinematics, a set of eight structure functions contribute to the polarization transfer [30,41]. In *noncoplanar*

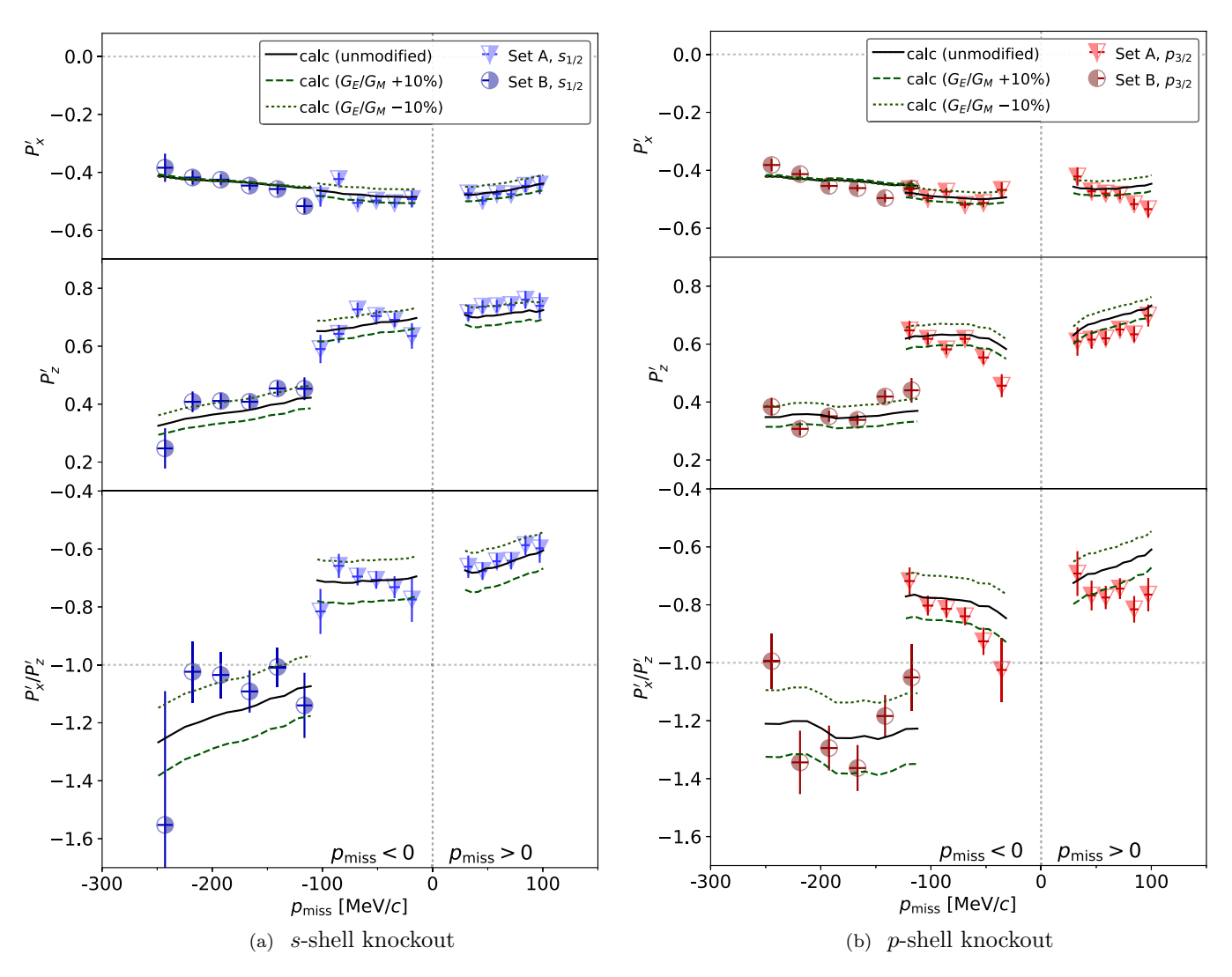


FIG. 7. DWIA calculations of the polarization observables, with unmodified FFs (solid curves), and with G_E/G_M scaled by +10% (-10%) shown as long-dashed (dotted) curves. These calculation curves are overlaid over the measured values from Fig. 6(a). These are shown separately for *s*-shell knockout (a) (blue) and *p*-shell knockout (b) (red).

kinematics, an additional structure function, $\bar{h}_{01}^{\prime N}$, contributes to P_x' but not P_z' .

The RDWIA program [31] was written to perform calculations only in the coplanar kinematics of the usual $A(\vec{e}, e'\vec{p})$ experiments. Therefore, it calculates only the structure functions that contribute in coplanar kinematics and not $\bar{h}_{01}^{\prime N}$. We performed calculations in noncoplanar kinematics using the approximation

$$\bar{h}_{01}^{\prime N} = -\bar{h}_{01}^{\prime S},\tag{9}$$

where \bar{h}_{01}^{S} is one of the structure functions calculated in [31]. Equation (9) is exactly true in parallel kinematics ($\theta_{pq} = 0$) [30], and we assume that it provides a valid approximation at small θ_{pq} , which dominate the kinematics of our data.

We averaged the polarizations calculated for the kinematics of a sample of events in each $p_{\rm miss}$ bin and show the results in Fig. 7 as solid curves, compared to our data. In order to examine the sensitivity of the calculations to the proton FFs,

we show as long-dashed (dotted) curves the results obtained with G_E/G_M rescaled by +(-)10%.

For Setting B, the curves for P'_x at $\pm 10\%$ are very close to the calculations for unmodified FFs, indicating that P'_x is not sensitive to the FF ratios in this region. This makes the P'_x at large p_{miss} useful for testing the agreement between the calculations and the data. By contrast, P'_z is strongly sensitive to the FF scaling. At Setting A, on the other hand, both P'_x and P'_z are sensitive to the scaling of the FF ratio.

For the s-shell knockout at both kinematic settings, there is excellent agreement between the calculations and the data, except in P'_z at large negative $p_{\rm miss}$ (Setting B), where they differ by about 10%. One may consider the possibility of scaling G_E/G_M in order to obtain a better fit to the data.

For the *p*-shell knockout, the calculations and the data are in decent agreement with each other, but the agreement is not as good as for the *s*-shell. Specifically, at Setting A, P'_z is overestimated by the calculations, while the magnitude of P'_x appears to be somewhat underestimated by the calculations.

Before quantifying the agreement between the calculations and the data, we discuss in Sec. V C the uncertainties and limitations of the calculations.

C. Uncertainties of the calculations

We have adopted a model (RDWIA) which is based on some assumptions and approximations which may affect the comparison with the data. Within the model there are uncertainties due to the choice of the different ingredients (bound-state wave functions, optical potentials, and proton form factors) that are adopted in the calculations. We evaluated the combined contribution to the uncertainty in the calculation due to the parametrizations of these ingredients to be 2.2%, 3.8%, and 4.0% for P_x' , P_z' , and P_x'/P_z' , respectively. These were obtained by adding the estimated contributions, as discussed in Sec. VB, from those three sources in quadrature. By far the largest contribution to this uncertainty comes from the choice of the optical potential.

In the calculations for the *p*-shell knockout, it is assumed that the ¹¹B residual nucleus is left in its ground state. The data include also the excited states, as shown in the measured missing-energy spectrum of Fig. 5. However, the majority of the p-shell contribution comes from the ground state and we have checked that the excited states do not strongly affect the data for p-shell knockout. Furthermore, the wave function of the p shell has a minimum at p = 0, possibly reducing the numerical accuracy of the calculations at low p_{miss} for this shell. The s-shell wave function does not have this problem, but the fact that in this case the A-1 system is in the continuum, while the DWIA model is in principle devised for discrete states, introduces an additional (although presumably reasonable) approximation. Finally, we note that in the calculations a relativistic mean-field approximation has been assumed. A more sophisticated model for nuclear structure may impact the results and improve the agreement with the experimental data.

D. Quantifying the agreement of the calculations with the data

To quantify the agreement between the calculations and the data, we use a bin-by-bin comparison, employing the χ^2 criterion:

$$\chi^{2} = \sum_{\substack{\alpha \in \{x, z\} \\ i \in \text{bins}}} \frac{\left(P_{\alpha, i}^{\prime \text{meas}} - P_{\alpha, i}^{\prime \text{calc}}\right)^{2}}{\left(dP_{\alpha, i}^{\prime \text{meas}}\right)^{2} + \left(dP_{\alpha, i}^{\prime \text{calc}}\right)^{2}},\tag{10}$$

where $P_{\alpha,i}^{\prime\,\text{meas}}$ and $P_{\alpha,i}^{\prime\,\text{calc}}$ are the measured and calculated values of the polarization transfer for a given axis, α (x and z), in the ith bin. The uncertainty in the measurement, $dP_{\alpha,i}^{\prime\,\text{meas}}$, includes the statistical error of the fit and the systematic uncertainty² added in quadrature. For $dP_{\alpha,i}^{\prime\,\text{calc}}$, we only included the errors of the calculation due to the parametrizations of the optical potential, wave function, and free-proton FFs (see Sec. V C), since the impacts of other effects on the calculations are undetermined. The χ^2 values are then converted to p values,

denoted by $p_{\text{val}}[\chi^2]$, where the number of degrees of freedom is twice the number of bins, as there is a measurement of P'_x and P'_z for each bin.

Scaling the FF ratio G_E/G_M has been suggested above in order to obtain a better fit to the data. In order to determine if this scaling improves the agreement between the calculations and the data, we varied the value of

$$a_{\text{mod}} \equiv \left(\frac{G_E}{G_M}\right)^{\text{bound}} / \left(\frac{G_E}{G_M}\right)^{\text{free}} - 1,$$
 (11)

and then reevaluated χ^2 and the p values. We determined the optimal values of a_{mod} which minimized the χ^2 separately for the s and p shells in each kinematic setting. The uncertainty on the fitted values of a_{mod} are given by

$$\delta a_{\text{mod}} = \left[\frac{\partial^2}{\partial a_{\text{mod}}^2} [\chi^2] \right]^{-1/2}, \tag{12}$$

evaluated where χ^2 is at its minimum. The results of these comparisons are given in Table III.

This comparison shows that the *s*-shell calculations at both kinematic settings agree with the data, even without scaling the FFs. At Setting B the optimized scaling $a_{\text{mod}} = -8.6\%$ improves the agreement for P'_z , while at Setting A there is no need of FF scaling.

The *p*-shell calculations, without and even with FF scaling, are generally in worse agreement with the data than those for the *s* shell. However, as shown in Table III, a scaling of $a_{\rm mod}=10.4\%$ at Setting A greatly improves the agreement with the data. This is an indication of either genuine modifications to the FFs, or of other possible effects which mimic a modification to the FFs. At Setting B, no FF scaling improves the agreement with the data.

VI. CONCLUSIONS

Measurements of the transverse and longitudinal components of the polarization transfer in the quasifree $^{12}\mathrm{C}(\vec{e},e'\vec{p})$ reaction have been presented and compared to RDWIA calculations. The comparison gives an overall good agreement, but some discrepancies are observed in s-shell knockout at large negative p_{miss} and in p-shell knockout.

For s-shell knockout, both P'_x and P'_z are in very good agreement with the data at low p_{miss} . P'_x is in good agreement with the data also at high p_{miss} . The only notable discrepancy for the s shell is that the calculations underestimate P'_z by about 10% at large negative p_{miss} . The s-shell knockout at large p_{miss} is a region of particular interest when searching for medium modifications to the form factors [20], because it has both the largest virtuality and the largest nuclear density in our dataset. We note that in this region P'_x is insensitive to G_E/G_M , and therefore the agreement between the calculated and measured P'_x gives further credibility to the calculations. Modifying the form-factor ratio in the calculations by -8.6% in this region improves their agreement with the data (by scaling P'_z while keeping P'_x unchanged).

For the *p*-shell knockout, the agreement with the data is not as good as for the *s* shell. At low p_{miss} , scaling the form-factor ratio by +10.4% greatly improves the agreement

²About 3% for both P'_r and P'_z ; see Table II.

With unmod. FFs With mod. FFs a_{mod} Shell Setting $p_{\rm val}[\chi^2]$ (%) $p_{\rm val}[\chi^2]$ n_{dof} 24 0.91 0.3 ± 2.5 23 0.89 A $s_{1/2}$ В 12 0.29 -8.6 ± 3.8 11 0.60 24 0.017 10.4 ± 2.6 23 0.37 Α $p_{3/2}$ R 12 0.049 -2.5 ± 3.1 0.04 11

TABLE III. The p values for the fits with unscaled and optimally scaled FFs. We also include the a_{mod} for the optimal scaling. The number of degrees of freedom for the comparison with scaled FFs is one fewer than for those with unscaled FFs.

with the data, which, however, remains worse than for the s shell. At high $p_{\rm miss}$, scaling the form-factor ratio does not improve the agreement with the data. Further theoretical work is required to understand the source of the discrepancies for p-shell knockout.

No global scaling to G_E/G_M , common to all kinematic regions in our dataset, would solve all the discrepancies. Scaling the form-factor ratio differently for each kinematic region leads to a good agreement between the data and calculations. We note, however, that form-factor modification is not the only possible solution. Other explanations can be envisaged and deserve further exploration.

From the experimental point of view, the large statistical errors at the large negative $p_{\rm miss}$ setting for both shells will be reduced by combining our data with those of a recent measurement from MAMI on 12 C at the same kinematic setting. The combined dataset could either improve the statistical significance of the deviations or show them to be statistical fluctuations.

Furthermore, the study of s-shell knockout in future experiments may be useful in search of medium modifications of

the nucleon form factors in nuclei. Such a measurement has been proposed at MAMI on ⁴⁰Ca [42]. Since the 1*s* shell has large virtuality in ⁴⁰Ca (similar to that of ¹²C), it would be a suitable nucleus with which to extend the searches for medium modifications.

ACKNOWLEDGMENTS

We would like to thank the Mainz Microtron operators and technical crew for the excellent operation of the accelerator. This work is supported by the Israel Science Foundation (Grants No. 390/15 and No. 951/19) of the Israel Academy of Arts and Sciences, by the PAZY Foundation (Grant No. 294/18), by the Israel Ministry of Science, Technology and Space, by the Deutsche Forschungsgemeinschaft (Collaborative Research Center 1044), and by the U.S. National Science Foundation (PHY-1205782). We acknowledge the financial support from the Slovenian Research Agency (research core funding No. P1–0102).

^[1] M. K. Jones *et al.* (Jefferson Lab Hall A Collaboration), G_{Ep}/G_{Mp} ratio by Polarization Transfer in Polarized $\vec{e}p \rightarrow e\vec{p}$, Phys. Rev. Lett. **84**, 1398 (2000).

^[2] O. Gayou *et al.* (Jefferson Lab Hall A Collaboration), Measurement of G_{Ep}/G_{Mp} in $\vec{e}p \rightarrow e\vec{p}$ to $Q^2 = 5.6 \text{ GeV}^2$, Phys. Rev. Lett. **88**, 092301 (2002).

^[3] V. Punjabi *et al.*, Proton elastic form-factor ratios to $Q^2 = 3.5 \text{ GeV}^2$ by polarization transfer, Phys. Rev. C **71**, 055202 (2005); **71**, 069902(E) (2005).

^[4] B. D. Milbrath, J. I. McIntyre, C. S. Armstrong, D. H. Barkhuff, W. Bertozzi, J. Chen *et al.* (Bates FPP Collaboration), A Comparison of Polarization Observables in Electron Scattering from the Proton and Deuteron, Phys. Rev. Lett. **80**, 452 (1998); **82**, 2221 (1999).

^[5] D. H. Barkhuff *et al.*, Measurement of recoil proton polarizations in the electrodisintegration of deuterium by polarized electrons, Phys. Lett. B 470, 39 (1999).

^[6] T. Pospischil *et al.* (A1 Collaboration), Measurement of G_{Ep}/G_{Mp} via polarization transfer at $Q^2 = 0.4(\text{GeV}/c)^2$, Eur. Phys. J. A **12**, 125 (2001).

^[7] O. Gayou, K. Wijesooriya *et al.* (The Jefferson Lab Hall A Collaboration), Measurements of the elastic electromagnetic

form factor ratio $\mu_p G_{\rm ep}/G_{\rm mp}$ via polarization transfer, Phys. Rev. C **64**, 038202 (2001).

^[8] G. MacLachlan *et al.*, The ratio of proton electromagnetic form factors via recoil polarimetry at $q^2 = 1.13 \text{ (GeV/}c)^2$, Nucl. Phys. A **764**, 261 (2006).

^[9] M. K. Jones *et al.* (Resonance Spin Structure Collaboration), Proton G_E/G_M from beam-target asymmetry, Phys. Rev. C **74**, 035201 (2006).

^[10] A. I. Akhiezer and M. Rekalo, Polarization effects in the scattering of leptons by hadrons, Fiz. Elem. Chastits At. Yadra 4, 662 (1973) [Sov. J. Part. Nucl. 4, 277 (1974)].

^[11] C. F. Perdrisat, V. Punjabi, and M. Vanderhaeghen, Nucleon electromagnetic form factors, Prog. Part. Nucl. Phys. 59, 694 (2007).

^[12] I. Yaron, D. Izraeli *et al.*, Polarization-transfer measurement to a large-virtuality bound proton in the deuteron, Phys. Lett. B 769, 21 (2017).

^[13] D. Izraeli, I. Yaron *et al.* (A1 Collaboration), Components of polarization-transfer to a bound proton in a deuteron measured by quasi-elastic electron scattering, Phys. Lett. B **781**, 107 (2018).

^[14] S. Paul, D. Izraeli, T. Brecelj, I. Yaron et al. (A1 Collaboration), Quasi-elastic polarization-transfer measurements on the

- deuteron in anti-parallel kinematics, Phys. Lett. B **795**, 599 (2019).
- [15] D. Izraeli, T. Brecelj *et al.* (A1 Collaboration), Measurement of polarization-transfer to bound protons in carbon and its virtuality dependence, Phys. Lett. B **781**, 95 (2018).
- [16] S. Strauch *et al.* (Jefferson Lab E93-049 Collaboration), Polarization Transfer in the ${}^{4}\text{He}(\vec{e}, e'\vec{p}){}^{3}\text{H}$ Reaction up to $Q^{2}=2.6$ (GeV/c)², Phys. Rev. Lett. **91**, 052301 (2003).
- [17] B. Hu *et al.*, Polarization transfer in the ${}^{2}\text{H}(\vec{e}, e'\vec{p})n$ reaction up to $Q^{2} = 1.61$ (GeV/c) 2 , Phys. Rev. C **73**, 064004 (2006).
- [18] M. Paolone, S. P. Malace, S. Strauch *et al.* (E03-104 Collaboration), Polarization Transfer in the ${}^{4}\text{He}(\vec{e},e'\vec{p})\,{}^{3}\text{H}$ Reaction at $Q^2=0.8$ and 1.3 $(\text{GeV}/c)^2$, Phys. Rev. Lett. **105**, 072001 (2010).
- [19] S. Paul, T. Brecelj, H. Arenhövel *et al.*, The influence of Fermi motion on the comparison of the polarization transfer to a proton in elastic *ep* and quasi-elastic *eA* scattering, Phys. Lett. B **792**, 445 (2019).
- [20] G. Ron, W. Cosyn, E. Piasetzky, J. Ryckebusch, and J. Lichtenstadt, Nuclear density dependence of in-medium polarization, Phys. Rev. C 87, 028202 (2013).
- [21] K. Blomqvist *et al.*, The three-spectrometer facility at MAMI, Nucl. Instrum. Methods A 403, 263 (1998).
- [22] B. Wagner, H. G. Andresen, K. H. Steffens, W. Hartmann, W. Heil, and E. Reichert, A Moller polarimeter for CW and pulsed intermediate-energy electron beams, Nucl. Instrum. Methods A 294, 541 (1990).
- [23] P. Bartsch, Aufbau eines Møller-polarimeters für die dreispektrometer-anlage und messung der helizitätsasymmetrie in der reaktion $p(e,e'p)\pi_0$ im bereich der Δ -resonanz, Ph.D. thesis, Institut für Kernphysik der Universität Mainz, 2001 (unpublished).
- [24] V. Tioukine, K. Aulenbacher, E. Riehn *et al.*, A Mott polarimeter operating at MeV electron beam energies, Rev. Sci. Instrum. 82, 033303 (2011).
- [25] T. Pospischil *et al.*, The focal plane proton-polarimeter for the 3-spectrometer setup at MAMI, Nucl. Instrum. Methods. Phys. Res., Sect. A **483**, 713 (2002).
- [26] D. Dutta *et al.*, Quasielastic (*e*, *e'p*) reaction on ¹²C, ⁵⁶Fe, and ¹⁹⁷Au, Phys. Rev. C **68**, 064603 (2003).
- [27] M. Distler, H. Merkel, and M. Weis, Data acquisition and analysis for the 3-spectrometer-setup at MAMI, in *Proceedings* of the 12th IEEE Real Time Congress on Nuclear and Plasma Sciences, Valencia, June 2001 (IEEE, Piscataway, NJ, 2001).

- [28] E. Aprile-Giboni, R. Hausammann, E. Heer, R. Hess, C. Lechanoine-Leluc, W. Leo, S. Morenzoni, Y. Onel, and D. Rapin, Proton-carbon effective analyzing power between 95 and 570 MeV, Nucl. Instrum. Methods 215, 147 (1983).
- [29] M. W. McNaughton et al., The p-C analyzing power between 100 and 750 MeV, Nucl. Instrum. Methods A 241, 435 (1985).
- [30] C. Giusti and F. D. Pacati, Complete determination of scattering amplitudes and nucleon polarization in electromagnetic knockout reactions, Nucl. Phys. A 504, 685 (1989).
- [31] A. Meucci, C. Giusti, and F. D. Pacati, Relativistic corrections in (e, e'p) knockout reactions, Phys. Rev. C **64**, 014604 (2001).
- [32] E. D. Cooper, S. Hama, and B. C. Clark, Global dirac optical potential from helium to lead, Phys. Rev. C 80, 034605 (2009).
- [33] E. D. Cooper, S. Hama, B. C. Clark, and R. L. Mercer, Global Dirac phenomenology for proton nucleus elastic scattering, Phys. Rev. C 47, 297 (1993).
- [34] W. Poschl, D. Vretenar, and P. Ring, Relativistic Hartree-Bogolyubov theory in coordinate space: Finite element solution for a nuclear system with spherical symmetry, Comput. Phys. Commun. 103, 217 (1997).
- [35] B. D. Serot and J. D. Walecka, The relativistic nuclear many body problem, Adv. Nucl. Phys. 16, 1 (1986).
- [36] B. D. Serot and J. D. Walecka, Recent progress in quantum hadrodynamics, Int. J. Mod. Phys. E 06, 515 (1997).
- [37] P. Ring, Relativistic mean field in finite nuclei, Prog. Part. Nucl. Phys. 37, 193 (1996).
- [38] G. A. Lalazissis, J. Konig, and P. Ring, A New parametrization for the Lagrangian density of relativistic mean field theory, Phys. Rev. C 55, 540 (1997).
- [39] M. Sharma, M. Nagarajan, and P. Ring, Rho meson coupling in the relativistic mean field theory and description of exotic nuclei, Phys. Lett. B 312, 377 (1993).
- [40] J. C. Bernauer, M. O. Distler, J. Friedrich, T. Walcher, P. Achenbach, C. Ayerbe-Gayoso *et al.* (A1 Collaboration), Electric and magnetic form factors of the proton, Phys. Rev. C 90, 015206 (2014).
- [41] S. Boffi, C. Giusti, F. d. Pacati, and M. Radici, *Electromagnetic Response of Atomic Nuclei*, Oxford Studies in Nuclear Physics Vol. 20 (Clarendon, Oxford, 1996).
- [42] P. Achenbach *et al.*, A1 MAMI Proposal: Polarization Transfer Measurements in ⁴⁰Ca(\vec{e} , $e'\vec{p}$) ³⁹K Scattering, 2018, S. Paul and U. Müller (spokespersons), https://wwwa1.kph.uni-mainz.de/A1/publications/proposals/MAMI-A1-1-18.pdf.